

The Highly Relativistic Kiloparsec-Scale Jet of the Gamma-Ray Quasar 0827+243

Svetlana G. Jorstad^{1,2} and Alan P. Marscher¹

ABSTRACT

We present *Chandra* X-ray (0.2-8 keV) and *Very Large Array* radio (15 and 5 GHz) images of the γ -ray bright, superluminal quasar 0827+243. The X-ray jet bends sharply—by $\sim 90^\circ$, presumably amplified by projection effects— $5''$ from the core. Only extremely weak radio emission is detected between the nuclear region and the bend. The X-ray continuum spectrum of the combined emission of the knots is rather flat, with a slope of -0.4 ± 0.2 , while the 5-15 GHz spectra are steeper for knots detected in the radio. These characteristics, as well as non-detection of the jet in the optical band by the *Hubble Space Telescope*, pose challenges to models for the spectral energy distributions (SEDs) of the jet features. The SEDs could arise from pure synchrotron emission from either a single or dual population of relativistic electrons only if the minimum electron energy per unit mass $\gamma_{\min} \gtrsim 1000$. In the case of a single population, the radiative energy losses of the X-ray emitting electrons must be suppressed owing to inverse Compton scattering in the Klein-Nishina regime, as proposed by Dermer & Atoyan. Alternatively, the X-ray emission could result from inverse Compton scattering of the Cosmic Microwave Background photons by electrons with Lorentz factors as low as $\gamma \sim 15$. In all models, the bulk Lorentz factor of the jet flow $\Gamma \gtrsim 20$ found on parsec scales must continue without substantial deceleration out to 800 kpc (deprojected) from the nucleus, and the magnetic field is very low, $\lesssim 2 \mu\text{G}$, until the bend. Deceleration does appear to occur at and beyond the sharp bend, such that the flow could be only mildly relativistic at the end of the jet. Significant intensification of the magnetic field occurs downstream of the bend, where there is an offset between the projected positions of the X-ray and radio features.

Subject headings: galaxies: quasars: general — galaxies: jets — galaxies: quasars: individual (0827+243) — X-rays: galaxies — radio continuum: galaxies

¹Institute for Astrophysical Research, Boston University, 725 Commonwealth Ave., Boston MA 02215

²Sobolev Astronomical Institute, St. Petersburg State University, 28 Universitetskij pr., St. Petersburg 198504 Russia

1. Introduction

Although the existence of X-ray emission in the jets of active galactic nuclei was known prior to the launch of the *Chandra* X-ray observatory, it was surprising to discover that a substantial fraction of observed kiloparsec-scale jets have detectable X-ray counterparts (e.g., Sambruna et al. 2004; Schwartz et al. 2003; Gelbord et al. 2003). In some cases—notably the Fanaroff-Riley I radio galaxies (e.g., Worrall, Birkinshaw, & Hardcastle 2001) and some quasars (Sambruna et al. 2004)—the multiwaveband spectra indicate that the X-ray emission is synchrotron radiation by electrons with energies $\gtrsim 1$ TeV. In others, inverse Compton scattering of the Cosmic Microwave Background (CMB) off ~ 0.1 GeV electrons in the jet (IC/CMB) provides an alternative X-ray emission mechanism (Tavecchio et al. 2000; Celotti, Ghisellini, & Chiaberge 2001; Sambruna et al. 2004). The synchrotron self-Compton process may be important in some condensed regions with high densities of relativistic electrons (see, e.g., Harris & Krawczynski 2002).

IC/CMB emission should be most pronounced in high-redshift objects with jets whose flow velocities remain highly relativistic out to scales of tens or hundreds of kiloparsecs, as long as one of the two opposing jets points almost directly along the line of sight. In this context γ -ray blazars, whose jets display faster apparent speeds than the general population of compact flat spectrum radio sources (Jorstad et al. 2001; Kellermann et al. 2004), are prime candidates for strong IC/CMB emission. Detection of IC/CMB X-rays provides a determination of the Doppler factor on kiloparsec scales (see Appendix A and Dermer & Atoyan 2004), which can then be compared with that measured on parsec scales. A number of kiloparsec scale jets show a decrease in the ratio of X-ray to radio intensity with distance from the core (Marshall et al. 2001; Siemiginowska et al. 2002; Sambruna et al. 2004). This could result from gradual decrease of the bulk Lorentz factor on kiloparsec scales (Georganopoulos & Kazanas 2004). Such a model can be tested only in the case of observation of multi-knot jet structure at two or more frequencies, which are rarely available despite the high sensitivity of Chandra observations. For these reasons, the detected X-ray/radio jet of the γ -ray bright quasar 0827+243 ($z = 0.939$; Hewitt & Burbidge 1993), which has apparent superluminal motion on millarcsecond scales as fast as $\beta_{\text{app}} \approx 22c$ (Jorstad et al. 2001), represents an excellent laboratory for studying the physical conditions in kiloparsec-scale jets.⁴

⁴An incorrect redshift was used by Jorstad et al. (2001), who followed the value given in Hartman et al. (1999). The apparent velocity given uses the correct redshift of 0.939. Proper motions are converted to speeds under a standard Friedmann cosmology with $H_0 = 70 \text{ km s}^{-1} \text{ Mpc}^{-1}$ and $q_0 = 0.1$. The conversion of angular to linear scale projected on the sky is then $1'' = 7.2 \text{ kpc}$.

2. Observations and Data Reduction

We have observed the quasar 0827+243 with the *Chandra* Advanced CCD Imaging Spectrometer (ACIS-S) at 0.2-8 keV and with the *Very Large Array* (VLA) interferometer of the National Radio Astronomy Observatory (NRAO) at 15.0 GHz (B array) and at 4.9 GHz (A array). This observational configuration provides similar resolution ($\sim 0''.5$) at all three frequencies. We have also retrieved an optical image of the quasar from the *Hubble Space Telescope* archive.

2.1. X-Ray Observations

We observed the quasar for 18.26 ks on 2002 May 10 with the ACIS-S detector of the *Chandra* X-Ray Observatory, using the back-illuminated S3 chip. In order to minimize the effect of pileup of the emission from the core, we used a 1/8 subarray to reduce the frame time to 0.4 s. The X-ray position of the quasar ($08^h30^m52^s.089,+24^\circ10'59''.67$, J2000) agrees very well with the radio position ($08^h30^m52^s.086,+24^\circ10'59''.82$). We used version 3.0.2 of the CIAO software and the version 2.26 of the CALDB calibration database for the data analysis. We generated a new level 2 event file to apply an updated gain map, to randomize the pulse height amplitude (PHA) values, and to remove the pixel randomization. We extracted the background by using four circular regions with radius $2''.5$ each on the east, north, west, and south sides at a distance $\sim 10''$ from the core, avoiding the readout streaks. We applied the pileup model in Sherpa to determine the pileup fraction of the core, 5.5%.

Figure 1 shows the smoothed image of the quasar in the range 0.2-8 keV. The image has a bright core and a jet that extends out to $\sim 6''.5$. At about $5''$ the jet, as defined by the emission, executes a sharp bend by $\sim 90^\circ$. The first section of the jet, between the core and the bend, is aligned with the direction of the parsec scale jet (Jorstad et al. 2001). The X-ray structure can be represented by three circular components ($C1$, $C2$, and $C3$) and an elliptical component ($C4$) with axial ratio ~ 0.6 . Table 1 gives extracted counts for the core, knots, and background. All knots are detected at a level of 6σ or higher relative to the background estimate. Table 1 shows that the hardness ratio peaks in the brightest jet component. We calculated the redistribution matrix and auxiliary response files for the core and jet regions using the thread *Extract ACIS Spectra for Pointlike Source and Make RMFs and ARFs*. We fit the spectral data for the core and jet in the range 0.2-8 keV in Sherpa by a power-law model with fixed Galactic absorption $N_H = 3.62 \times 10^{20}$ corresponding to the direction of the quasar, obtained with routine COLDEN based on the data of Dickey & Lockman (1990). The best-fit photon indices are very similar for the core and extended jet, 1.34 ± 0.02 and 1.4 ± 0.2 , respectively. This is consistent with the flat X-ray spectra of bright jet knots found

previously in other quasars (Sambruna et al. 2004; Siemiginowska et al. 2002). The jet emits a fraction ~ 0.01 of the apparent core luminosity $L_{core} = (1.16 \pm 0.07) \times 10^{46}$ erg s $^{-1}$ over the energy range 0.2-8 keV. We calculated the flux of the individual jet components at 1 keV (see Table 2) after fixing the jet power-law photon index at 1.4 and the Galactic absorption as indicated above.

We used the *Chandra* Ray Tracer facility to produce a point spread function (PSF) to match the core region. The PSF was calculated for the position of the core, its spectrum at 0.2-8 keV, and the exposure time. The PSF was projected onto the detector using a thread in the MARX program. A subpixelated image of the PSF was created by following the thread *Creating an Image of the PSF* in CIAO. The resulting image is displayed in Figure 1.

2.2. Radio Observations

We performed observations with the *Very Large Array* (VLA) of the National Radio Astronomy Observatory (NRAO) at 15 GHz (central frequency = 14.9649 GHz, bandwidth = 50 MHz) in B array on 2002 August 19, and at 5 GHz (central frequency = 4.86010 GHz, bandwidth = 50 MHz) in A array on 2003 August 28. We edited and calibrated the data using the Astronomical Image Processing System (AIPS) software provided by NRAO. The resulting images are shown in Figure 2. Although the resolution of the VLA observations $\sim 0''.4$, we convolved the images with a circular Gaussian beam of FWHM = $0''.5$ in order to match the resolution of the *Chandra* images. We modeled the total and polarized intensity images with circular Gaussian components using the software Difmap (Shepherd 1997) and IDL (by Research Systems, Inc.), respectively.

The core has an inverted radio spectrum and is linearly polarized at 5 GHz at a level of $4.5 \pm 0.5\%$ with electric vector position angle (EVPA) of 43° , roughly transverse to the main parsec-scale jet direction (Jorstad et al. 2001). At 15 GHz the core has a more modest fractional polarization ($1.8 \pm 0.7\%$) with EVPA = 116° . The latter is close to the direction and EVPA of the innermost jet just outside the parsec-scale core before it bends toward the kiloparsec-scale structure (Marscher et al. 2002; Jorstad et al. 2001). The difference in polarization at the two frequencies might be due to variability of the core radio emission, since the VLA observations were separated by 1 yr.

The images reveal very interesting structure of the kiloparsec-scale jet: (i) knot *B1*, $\sim 0''.4$ from the core, has a position angle corresponding to that of the main parsec-scale jet (Jorstad et al. 2001); (ii) despite high dynamic range (RMS < 0.1 mJy), neither the 5 GHz nor 15 GHz image shows significant radio emission between $\sim 0''.5$ and $5''$ from the core where

the brightest X-ray features are observed; and (iii) the large-scale radio jet starts beyond $5''$ and is roughly perpendicular to the parsec-scale jet as projected on the sky, corresponding to the direction of the second section of the extended X-ray structure. The 5-15 GHz spectral index α (flux density $S_\nu \propto \nu^{-\alpha}$) of the knots generally increases with distance from the core, from ~ 0.7 (*B1*) to ~ 1.1 (*C5*). However, the brightest radio feature, *C6*, at the edge of the kiloparsec-scale jet has a radio spectral index $\alpha \sim 0.8$ and is highly polarized ($20 \pm 5\%$), with EVPA parallel (magnetic field perpendicular) to the local jet direction. Curiously, feature *C3* near the bend is detected at 5 GHz but not at 15 GHz, which requires an extremely steep spectrum, $\alpha \geq 1.5$.

2.3. Optical Data

A field containing 0827+243 was observed by Steidel et al. (2002) with the Wide Field Planetary Camera 2 (WFPC2) of the *Hubble Space Telescope* (HST) as a part of a survey of QSO-absorbing galaxies at intermediate redshifts. We retrieved the images of this field from the HST archive. The images were obtained in the F702W ($\lambda_{\text{eff}} = 708.14$ nm) filter on 1995 May 29 with a total exposure of 4.6 ks, and calibrated by the HST standard processing pipeline. We used the European Southern Observatory image reduction software MIDAS to analyze the images (draw profiles and measure magnitudes). We applied the absolute flux calibration given in the headers of the images and in the WFPC2 Instrument Handbook to convert the instrumental magnitudes to fluxes.

Figure 3 traces the optical profiles along the X-ray jet (*a*) and two rays, *b* and *c*, in the counterjet direction and perpendicular to the jet-counterjet line, respectively. The *a* profile shows a slight increase in the number of counts in the region of the brightest X-ray component *C2*, but at an insignificant level. The estimated 1σ upper limits are 2.5×10^{-30} erg cm $^{-2}$ s $^{-1}$ Hz $^{-1}$ for *C2* and 2.1×10^{-30} erg cm $^{-2}$ s $^{-1}$ Hz $^{-1}$ for *C1*, *C3*, *C4*, *C5*, and *C6*.

3. Properties of the X-Ray/Radio Jet Emission

The most striking features of the combined X-ray and radio images (Fig. 4) are the strong bend in the kiloparsec-scale jet and the absence of detected radio emission over much of the X-ray bright section. The X-ray emission in 0827+243 extends about $5''.5$ from the core, then executes a bend of $\sim 90^\circ$ in projection on the sky. Beyond this point, the X-ray jet continues for about $2''$. Outside the nuclear region, the radio emission first rises above the noise level only near the bend. The direction of the inner X-ray jet is within 5° of that

of the parsec-scale radio jet, where Jorstad et al. (2001) have measured apparent speeds as high as $\beta_{\text{app}} = 22 \pm 2c$. This apparent speed implies that the bulk Lorentz factor $\Gamma \geq 22$, with an optimal viewing angle $\theta \leq 2^\circ.5$. Using the least extreme values of Γ and θ provides an estimate of the Doppler factor on parsec scales, $\delta \equiv [\Gamma(1 - \beta \cos \theta)]^{-1} \sim \Gamma \approx 22$, where β is the actual bulk velocity in units of c .

Figure 5 displays the inner region of the X-ray/radio jet after subtracting the PSF from the core. Two new components close to the core, $B1$ and $B2$, are apparent in the X-ray jet (of these only knot $B1$ is detected in the radio), aligned to within 2° of the main parsec-scale structure. When projection effects are considered, this indicates an essentially linear continuation from parsec to kiloparsec scales up to the sharp-angle bend. Table 2 lists the parameters of the kiloparsec-scale jet features at 1 keV and 5 GHz. Figure 6 shows the X-ray and radio intensity profiles along the jet axis as indicated in Figure 1 after core subtraction, as well as the spectral index variation along the jet.

The profiles displayed in Figure 6 show clearly the fading of the X-ray emission with distance from the nucleus while the radio intensity increases. Similar X-ray/radio intensity-ratio gradients are found in several other quasars (3C 273, Marshall et al. 2001; PKS 1127–145, Siemiginowska et al. 2002; PKS 1136–135 and PKS 1510–089, Sambruna et al. 2004), while in the majority of jets detected by *Chandra* the X-ray knots coincide with bright radio features (Sambruna et al. 2004). Note that 3C 273, PKS 1127–145, PKS 1510–089, and 0827+243 are all γ -ray bright quasars with high apparent speeds ($\gtrsim 10c$) on parsec scales (Jorstad et al. 2001).

Because of limited photon statistics, the angular sizes determined from the X-ray image are uncertain by $\sim 50\%$. Similarly, the offsets of the X-ray and radio intensity apparent in Figs. 4 and 5 in features $C3$ and $C4$ may not be real. The presence of any X-ray photons outside the core region *is* highly significant, but the absence of such photons near the periphery of a knot could be due to either a genuine lack of emission or insufficient exposure time.

In order to produce an apparent bend of 90° , the jet would need to change its intrinsic direction by an angle at least equal to the initial viewing angle. Since this is only $\sim 2^\circ.5$, the intrinsic change in trajectory can be quite modest. The bend could be caused by deflection of the jet flow by a cloud, in which case one would expect a standing shock wave to compress and heat the jet plasma while it decelerates the bulk motion. The observed drop in intensity around the bend (see Fig. 6) implies that the decrease in Doppler beaming more strongly influences the observed emission than does the compression and heating.

An alternative scenario for the apparent bending is that the jet flow has always been

straight, but the direction of the “nozzle” changed. That is, about 4×10^6 yr in the past the jet might have pointed from the nucleus to knot $C6$, then steadily swung until it reached its current direction about 2.5×10^6 yr ago. In this case, knots $C4$, $C5$, and $C6$ could no longer be energized by the jet. The radiative lifetime of electrons emitting at a frequency $\nu_{s,\text{GHz}}$ GHz is

$$t_{\text{loss}} \approx 1.3 \times 10^6 \left(\frac{B_{\mu\text{G}} \delta}{\nu_{s,\text{GHz}}(1+z)} \right)^{1/2} [B_{\mu\text{G}}^2 + 11(1+z)^4 \Gamma^2]^{-1} \text{ yr}, \quad (1)$$

where the quantities on the right-hand side are all defined in Appendix A. This includes energy losses to both synchrotron radiation and IC/CMB scattering in the Thomson limit. For the magnetic fields we derive in the next section, the lifetimes of electrons (times the bulk Lorentz factor Γ to translate to the rest frame of the host galaxy) radiating at 15 GHz are considerably shorter than the estimated age of knot $C6$, $\gtrsim 4 \times 10^6$ yr.

4. The Nature of X-ray Emission in the Large-Scale Jet

The most popular models to explain the observed spectral energy distribution (SED) of features on kiloparsec scales involve (1) synchrotron radiation from a single population (Marshall et al. 2001; Harris & Krawczynski 2002; Dermer & Atoyan 2002) or dual population (Harris & Krawczynski 2002; Atoyan & Dermer 2004; Sambruna et al. 2004) of relativistic electrons, and/or (2) inverse-Compton scattering off the Cosmic Microwave Background (IC/CMB, Tavecchio et al. 2000; Celotti, Ghisellini, & Chiaberge 2001). The detection of several X-ray knots at different distances from the core allows us to constrain the possible emission processes, and then to derive key physical parameters and how they vary as a function of distance from the nucleus.

Measurements of the radio synchrotron emission determine the value of the product $B\delta$, or an upper limit for knots that are not detected at either 5 or 15 GHz, through eq. (A3). This product depends on the unknown quantities k , A , and ϕ , which represent the ratio of proton to electron energy density, the ratio of particle to magnetic energy density, and volume filling factor, respectively. However, these are raised to a small power, hence only unlikely, extreme values of these parameters could affect greatly the derived value of $B\delta$. The models for the X-ray emission from the jet of 0827+243 must therefore be consistent with the values or limits to $B\delta$ dictated by the observations.

Figure 7 shows the observed spectral energy distributions (SEDs) for the three most prominent regions in the jet: knot $C2$, with the brightest X-ray emission and non-detection at optical and radio frequencies, $C4$, with measured X-ray and radio fluxes and optical upper limit, and $C6$, detected only in the radio. The X-ray spectral index, $\alpha_x = 0.4 \pm 0.2$,

is significantly flatter than the radio spectral indices, $\alpha_r = 0.7-1.1$. (As discussed above, there are only enough photon counts to determine the X-ray spectral index for all the knots combined. Therefore, it is possible for one knot to have a steeper spectrum, but not all.) This places further constraints on the emission models, such that a simple power-law energy distribution of a single population of electrons is not viable. We now discuss models in which the X-ray emission is either synchrotron radiation or upscattered CMB photons.

4.1. Synchrotron Model

The SEDs of *C2* and *C6* are each consistent with synchrotron emission from a single population of relativistic electrons. However, either the slopes of the electron energy distributions of the two knots are different or the SED contains a hump at X-ray frequencies owing to inefficient inverse Compton cooling of CMB photons in the Klein-Nishina regime (Dermer & Atoyan 2002; Atoyan & Dermer 2004). Because the optical upper limit falls below the extrapolation of the radio spectrum, the SED of knot *C4* can be fit by synchrotron emission from a single electron population only under the Dermer & Atoyan (2002) scheme. In order to fit SEDs similar to those of knots *C2* and *C4*, one needs to adopt a very high value ($\gtrsim 1000$) of the “minimum” electron Lorentz factor γ_{\min} . This can represent either a lower-energy cut-off or the energy above which the power-law energy distribution breaks to a slope steeper than -2 . On the other hand, relativistic shock waves should heat electron-proton plasmas to an average thermal energy per particle $\sim \Gamma'_s m_p c^2$ (Blandford & McKee 1977), where m_p is the rest mass of a proton and Γ'_s is the bulk Lorentz factor of the shock front in the co-moving frame of the unshocked jet. Hence, $\gamma_{\min} \sim 2000\Gamma'_s$ is expected in the co-moving frame of the emitting plasma.

The main difficulty in applying the Dermer & Atoyan (2002) model to 0827+243 is the poor match at the low-frequency end of the SED. Knot *C4* has a steeper radio spectral index than that of the model SEDs. In addition, the low radio flux of knot *C2* is expected only for very short times since the onset of particle acceleration, $\lesssim 10^3$ yr as measured in the co-moving frame. On the other hand, the latter condition can be met if the bulk Lorentz factor $\Gamma \gtrsim 20$, since the measured diameter of *C2* of 5 kpc implies a lifetime of at least $2 \times 10^4 \Gamma^{-1}$ yr in the co-moving frame. The SEDs of the knots of 0827+243 then require $\gamma_{\min} \gtrsim 10^3$ in order to avoid the dominance of IC/CMB emission over synchrotron radiation at X-ray energies.

Alternatively, all of the observed SEDs could be explained through synchrotron radiation from two populations of relativistic electrons, plausibly associated with jet structure transverse to the axis, as in spine-sheath models (e.g. Laing et al. 1999). The physical parameters

of the plasma corresponding to these two populations are given in Table 3. They are computed with eq. (A3) under the assumptions that each population is in energy equipartition with the magnetic field ($A = 1$), the kinetic energy in protons and electrons is comparable ($k = 1$), and the emission fills the entire structure ($\phi = 1$). The simulated SEDs are shown in Figure 7. Constraints on the spine population are similar to those of the Dermer & Atoyan (2002) model, hence $\Gamma \gtrsim 20$ is needed and the X-ray spectrum is flattened because the dominant process by which the electrons cool is IC/CMB scattering in the Klein-Nishina limit. In this case, the energy loss rate depends on electron Lorentz factor as $\sim \gamma^{0.3}$ (Dermer & Atoyan 2002). Therefore, the spine is populated by high-energy electrons with Lorentz factors $10^3 \leq \gamma \leq 3 \times 10^8$, flat spectral energy distribution, $\alpha \sim 0.4$, Doppler factor $\delta \sim 20$, and low magnetic field, $B \sim 0.5 \mu\text{G}$. This value of γ_{max} is the minimum capable of producing the observed X-ray flux via the synchrotron mechanism given the derived strength of the magnetic field.

The sheath in this model has $\gamma_{\text{max}} \sim 5 \times 10^5$ and a steep spectral index, $\alpha \sim 1.5$, and is less relativistic ($\delta \sim 2 - 5$, although this is not well specified in the model) with a higher magnetic field, $B \sim 20\text{-}100 \mu\text{G}$. The range of possible values of γ_{max} allows the synchrotron power-law spectrum to extend to 15 GHz but not to 420 THz in the optical region. The value of the minimum electron Lorentz factor is uncertain; that given in Table 3 fits the SEDs without excessive energy requirements. Kelvin-Helmholtz instabilities should generate turbulence between the spine and sheath, leading to cooling and deceleration of the spine and an increase in the internal energy of the sheath. We expect that this could accelerate electrons to achieve a flatter spectrum in the sheath as the turbulence develops along the jet. In this model the spine produces the X-rays and the sheath generates the radio emission that we observe. Since the X-ray and radio emission regions are not co-spatial, the features with detected X-ray and radio emission might appear shifted relative to each other. An apparent offset of $\sim 0.4''$ is in fact observed in the case of knot *C3* (see Fig. 4), which is especially interesting if real because the shift is primarily perpendicular to the jet axis.

4.2. Inverse Compton Scattering off the Cosmic Microwave Background

Inverse Compton scattering off CMB photons is a potentially efficient way to produce extended X-ray emission (Tavecchio et al. 2000; Celotti, Ghisellini, & Chiaberge 2001). If the mechanism dominates in a kiloparsec-scale jet, as deduced in a number of objects by Sambruna et al. (2004), the high-energy photon spectrum is expected to extend up to the γ -ray domain. As is discussed by the above authors (see also eq. A5 in Appendix A), IC/CMB can dominate the X-ray emission if the Doppler factor and redshift are high. In the case

of the quasar 0827+243, a number of properties of the jet indicate that the Doppler factor remains high out to the X-ray knots: (1) the X-ray jet aligns with the parsec-scale jet, where highly superluminal apparent speed, $\beta_{app} = (22 \pm 2)c$, is found (Jorstad et al. 2001); ii) the sharp bend of the X-ray jet is almost surely amplified owing to a small angle between the jet axis and line of sight (see above); iii) the decrease of X-ray to radio intensity ratio along the jet can be attributed to deceleration of the jet from an initially very high bulk Lorentz factor Γ (see Georganopoulos & Kazanas 2004).

Figure 8 shows the observed and simulated SEDs for components $C2$, $C4$, and $C6$. The simulated SEDs are combined synchrotron and IC/CMB emission from a single population of relativistic electrons with $\gamma_{min} = 15$ and $\gamma_{max} = 5 \times 10^5$. The value of γ_{max} should not be higher and γ_{min} should not be lower than the indicated values, otherwise we would expect these knots to be detected at optical wavelengths. The value of γ_{min} cannot be greater than 15 without causing the low-frequency cutoff to the X-ray spectrum to exceed the soft band of our *Chandra* observation. Because we have no measurements of α_x and α_r in the same feature (knots $C3$ and $C4$ are too faint to estimate the X-ray spectral index separately from $C1$ and $C2$), we consider that $\alpha_x = \alpha_r$, as expected for IC/CMB emission when the same power-law distribution of scattering electrons also produces the radio emission. We could also obtain α_x flatter than α_r if we were to assume that the electron energy distribution breaks from a slope of -1.8 below $\gamma \sim 2000$ to a slope steeper than -3 at higher energies; see the previous section.

The IC/CMB X-ray model combined with synchrotron radio emission allows us to estimate the parameters of the jet using eq. (A7), (A5), and (A3). Equation (A7) provides an estimate for (or limit to) the ratio δB^{-1} , while eq. (A3) and (A5) give the values of (or limits to) the products $B\delta$ and $B\delta^{\alpha+2}$ for the radio synchrotron and X-ray IC/CMB emission, respectively. Table 4 presents the parameters derived for each jet feature. The model fits the observed spectral energy distribution quite well (Fig. 8) except that the X-ray spectrum of knot $C4$ is much steeper than the combined spectrum of all the X-ray knots. This can be accommodated by the data, since $C4$ contains only about 18% of the X-ray flux from the extended jet. It is also consistent with low-energy flattening of the electron energy distribution, as discussed above. Knot $C2$ has marginally detected radio emission at 5 GHz (Fig. 4) that matches the flux of the model SED.

One striking property of the model is that the Doppler factor δ of X-ray features $B2$, $C1$, and $C2$ coincides with the estimate of the parsec-scale δ based on the apparent speed. Moreover, since the X-ray and parsec-scale radio jets lie in the same direction, there is no evidence of bending that would change the angle $\theta \lesssim 2^\circ 5$ between the jet axis and the line of sight. This strongly implies that the bulk Lorentz factor remains constant from parsec to

kiloparsec scales and that the magnetic field is very low, $B \approx 2 \mu\text{G}$, upstream of the bend. These conclusions would be modified somewhat if a dual population of electrons were to exist in a given knot such that the X-rays were a roughly equal combination of synchrotron and IC/CMB emission. In this case, $\delta \sim 7.5$ and $B \sim 3 \mu\text{G}$ would be possible before the bend. It is doubtful, however, that such a balance between the two emission mechanisms would occur for all three knots upstream of the bend.

According to the model parameters, deceleration of the jet does occur after the sharp bend beyond component *C2*, as anticipated from hydrodynamic considerations. The decrease in bulk Lorentz factor is accompanied by intensification of the magnetic field. As has been discussed by Georganopoulos & Kazanas (2004), this is expected for a decelerating relativistic jet, since the magnetic field in the co-moving frame of the emitting plasma $B \propto B_*/\Gamma$, where B_* is the magnetic field in the rest frame of the host galaxy of the quasar. We note that these inferences are independent of the nature of the X-ray emission, but do assume that the equipartition condition holds. The significant change in the projected direction of the jet implies that the variation in δ is influenced both by a decrease in Γ and a change in θ . The apparent bending requires a change $\Delta\theta \geq \theta$, but it would be difficult to deflect a powerful, highly relativistic jet by more than a few degrees while conserving momentum. Hence, we can assume that the new viewing angle $\theta(\text{post-bend}) \approx 5^\circ$. As shown in Figure 9, the value of Γ after the bend is then roughly equal to half the Doppler factor. Therefore, the decrease in the Doppler factor is primarily a consequence of deceleration of the jet flow.

Further evidence for deceleration of the jet flow is found in the shift between the X-ray and radio positions of component *C3* and in the existence of an extended radio tail downstream of knot *C4* (see Fig. 4), in qualitative agreement with numerical simulations of a decelerating jet (cf. Fig. 2 in Georganopoulos & Kazanas 2004).

The required kinetic luminosities of the X-ray emitting knots are high, but perhaps possible for a powerful jet, $\sim 7 \times 10^{47} \text{ erg s}^{-1}$ for *C3*, $\sim 6 \times 10^{47} \text{ erg s}^{-1}$ for *C4*, and less for the others, when the bulk kinetic energy of the protons is included. These values argue that the jet cannot be far from equipartition between the energy density of relativistic electrons and that of the magnetic field. Otherwise, the required luminosities would be excessive (see Atoyan & Dermer 2004; Dermer & Atoyan 2004). If the positively charged particles are mainly positrons, the luminosities are quite reasonable, $\lesssim 10^{46} \text{ erg s}^{-1}$, and some departure from equipartition would be possible. The required kinetic luminosities of knots *C3* and *C4* could also be reduced below $3 \times 10^{46} \text{ erg s}^{-1}$ if there is a break in the electron energy distribution at $\gamma_{\text{break}} \sim 2000$, in which case γ_{min} in eq. (A3) should be replaced by γ_{break} . As mentioned above, this can explain the flat X-ray spectra alongside the steeper radio spectra.

5. Conclusions

The relatively flat X-ray spectrum of the extended jet of 0827+243 is consistent with synchrotron radiation from extremely high-energy electrons under the Dermer & Atoyan (2002) scenario or within a dual population (e.g., spine-sheath) model. It can also be explained by inverse Compton scattering of CMB photons by $\gamma \sim 15$ electrons if the energy distribution of the electrons is relatively flat below $\gamma \sim 10^3$ and steeper above this value. All models require very high Doppler factors, consistent with the value $\delta \approx 20$ inferred from the parsec-scale superluminal apparent motion, and very low magnetic field ($\lesssim 2 \mu\text{G}$) upstream of the bend situated $5''$ from the core. The implication is that the bulk Lorentz factor of the jet flow maintains its high value all the way from parsec scales to ~ 800 kpc from the nucleus. Beyond this point, the jet bends by about 90° projected on the sky and at least 2.4 in three dimensions. In the IC/CMB model, the flow decelerates while the magnetic field intensifies at and beyond the bend. The latter follows the expectations of the model of Georganopoulos & Kazanas (2004), although the jump in field strength at the bend is about 4 times greater than the model predicts. This is in line with the supposition that a standing shock accompanies the bend in the flow.

In the IC/CMB case and in most of the synchrotron models, the energetics of the jet are reasonable if the energy distribution of the electrons is less steep than $\propto \gamma^{-2}$ below a rather high value of γ , ~ 1000 . Such high break energies are consistent with particle acceleration by relativistic shocks. Other possible processes for producing high values of γ_{min} are discussed by Gopal-Krishna, Biermann, & Wiita (2004). As mentioned by Georganopoulos & Kazanas (2004), the Dermer & Atoyan (2002) proposal predicts that the sizes of X-ray knots should be smaller than those of optical knots owing to the more severe energy losses of X-ray emitting electrons. However, we detect no optical knots in 0827+243, and hence cannot apply this test with our current data.

The flat spectrum of the X-ray jet features suggests that the maximum energy output of the knots could occur in the γ -ray domain, perhaps up to the TeV region ($\nu \sim 10^{25}$ Hz), although this emission is difficult to observe. TeV photons from such a high redshift ($z = 0.939$) will pair-produce off cosmic infrared photons before reaching the Earth. In addition, current γ -ray detectors have insufficient resolution to isolate any emission from the extended jet, and the nuclear emission probably dominates the total γ -ray flux. Nevertheless, the γ -ray flux should not be observed to drop below the expected level if the models are valid. At lower frequencies, synchrotron and, for knots with low values of δ , IC/CMB emission could contribute substantial amounts of optical and infrared flux from the jet in 0827+243. Observations in these wavebands could define the lower and/or upper cutoffs of the relativistic electron energy distributions, thereby removing one of the remaining ambiguities in our

analysis.

A. Derivation of Magnetic Field and Doppler Factor from X-ray and Radio Observations

A.1. Relations for Synchrotron Emission

If the dominant contribution to the observed flux density at a given frequency can be identified as synchrotron radiation, we can relate the magnetic field strength B and Doppler factor δ to observed parameters as follows. Based on the formulas given in Pacholczyk (1970), Marscher (1983) expressed the synchrotron flux density F_ν at frequency ν_s as

$$F_s(\nu_s) = c_1(\alpha) D_\ell^{-2} N_0 B^{1+\alpha} V \delta^{3+\alpha} (1+z)^{1-\alpha} \nu_s^{-\alpha}, \quad (\text{A1})$$

where $c_1(\alpha)$ is tabulated in Table A1, D_ℓ is the luminosity distance, and N_0 and α define the electron energy distribution, $N(E) = N_0 E^{-(1+2\alpha)}$. The volume of the emitting region $V = (4\pi/3)R^3\phi$ if the source is approximated as a sphere with a volume filling factor ϕ .

The quantity N_0 can be related to the magnetic field B through the ratio of particle to magnetic energy density A and the fraction k of the particle energy contained in non-electrons (where positrons are considered as electrons). Equipartition in energy between particles and magnetic field corresponds to $A = 1$. By integrating over $N(E)$ to determine the energy density in electrons and relating this to the magnetic energy density $B^2/(8\pi)$, we find that

$$N_0 = \frac{A(mc^2)^{2\alpha-1}}{8\pi(1+k)} g(\alpha, \gamma_{\min}, \gamma_{\max})^{-1} B^2, \quad (\text{A2})$$

where $g(\alpha, \gamma_{\min}, \gamma_{\max}) \equiv (2\alpha - 1)^{-1} [\gamma_{\min}^{1-2\alpha} - \gamma_{\max}^{1-2\alpha}]$ except for the special case $\alpha = 0.5$, for which $g = \ln(\gamma_{\max}/\gamma_{\min})$.

We can express the radius R in terms of the angular diameter Θ_{as} arcsec, redshift z , and luminosity distance D_{Gpc} Gpc, as $R = 2.42\Theta_{\text{as}}D_{\text{Gpc}}(1+z)^{-2}$ kpc. Inserting the above relations into (A1) and converting to convenient units as denoted by subscripts, we obtain the value of the magnetic field that corresponds to the observed flux density of synchrotron emission:

$$B = c_4(\alpha) \delta^{-1} (1+z)^{(5+\alpha)/(3+\alpha)} \left[\frac{(1+k)}{A\phi} g(\alpha, \gamma_{\min}, \gamma_{\max}) D_{\text{Gpc}}^{-1} \Theta_{\text{as}}^{-3} F_{\text{s,mJy}} \nu_{\text{s,GHz}}^\alpha \right]^{1/(3+\alpha)} \mu\text{G}. \quad (\text{A3})$$

The function $c_4(\alpha)$ is tabulated in Table A1.

A.2. Combined Inverse Compton and Synchrotron Relations

The flux density of inverse Compton emission at frequency ν_{IC} from a population of electrons with a power-law energy distribution scattering a monochromatic field of seed photons of frequency ν_{seed} and energy density u_{seed} is

$$F_{\text{IC}} = c_2(\alpha) \frac{u_{\text{seed}}}{\nu_{\text{seed}}} D_\ell^{-2} N_0 V \delta^{4+2\alpha} (1+z)^{1-\alpha} (\nu_{\text{IC}}/\nu_{\text{seed}})^{-\alpha}. \quad (\text{A4})$$

Here, $c_2(\alpha) \equiv (c\sigma_{\text{T}}/2)(mc^2)^{-2\alpha}$, where c is the speed of light, m is the mass of the electron, and σ_{T} is the Thomson cross-section. In order to derive equation (A5), we started with the inverse Compton formula of Dermer (1995) and applied relation (A2).

In the case of IC/CMB emission, $u_{\text{seed}} = 4.2 \times 10^{-13}(1+z)^4 \text{ erg cm}^{-3}$ and $\nu_{\text{seed}} = 5.7 \times 10^{10}(1+z) \text{ Hz}$. Use of these values in eq. (A4) and conversion to convenient units gives

$$F_{\text{IC/CMB}} = \frac{c_5(\alpha) A \phi}{1+k} g(\alpha, \gamma_{\text{min}}, \gamma_{\text{max}})^{-1} D_{\text{Gpc}} \Theta_{\text{as}}^3 B_{\mu\text{G}}^2 \delta^{4+2\alpha} (1+z)^{-2} E_{\text{IC,keV}}^{-\alpha} \text{ nJy}, \quad (\text{A5})$$

where $B_{\mu\text{G}}$ is the magnetic field in μG and $E_{\text{IC,keV}}$ is the observed scattered photon energy in keV. The function $c_5(\alpha) \equiv 0.063(4.2 \times 10^6)^{-\alpha} f(\alpha)$, where $f(\alpha)$ is a factor that corrects for the use of a monochromatic seed photon field rather than a Planck function in the derivation of eq. (A5). We tabulate both c_5 and f , the latter of which we have calculated through numerical integration, in Table A1. Note that the inverse proportionality between the IC/CMB flux density and the redshift term is due to the conversion of linear size to angular size. For a fixed volume of the emission region, the IC/CMB flux density varies as $(1+z)^4$.

We can substitute expression (A3) for $B_{\mu\text{G}}$ into equation (A5) and solve for the Doppler factor in terms of observable quantities and the function $g(\alpha, \gamma_{\text{min}}, \gamma_{\text{max}})$:

$$\delta = 10c_6(\alpha) \left[\frac{(1+k)}{A\phi} g(\alpha, \gamma_{\text{min}}, \gamma_{\text{max}}) D_{\text{Gpc}}^{-1} \Theta_{\text{as}}^{-3} \right]^{1/[2(3+\alpha)]} [F_{\text{s,mJy}} \nu_{\text{s,GHz}}^\alpha (1+z)^2]^{-1/[(1+\alpha)(3+\alpha)]} \times \\ \times [F_{\text{IC/CMB,nJy}}(\nu_{\text{IC}}) E_{\text{IC,keV}}^\alpha]^{1/[2(1+\alpha)]}. \quad (\text{A6})$$

The function $c_6(\alpha)$, which is of order unity, is listed in Table A1. The exponent $1/[2(3+\alpha)]$ ranges from 0.16 to 0.11 for the values of α considered here (0.2 to 1.5), hence the dependence of the derived Doppler factor on the poorly known quantity $g(\alpha, \gamma_{\text{min}}, \gamma_{\text{max}})$ is quite weak.

If the dominant X-ray emission mechanism of a knot is IC/CMB, we can combine equations (A1) and (A5) to form the ratio of the X-ray IC/CMB flux density at photon energy E_{keV} keV to the synchrotron flux density at frequency $\nu_{\text{s,GHz}}$ GHz. This produces a formula involving B and δ that is independent of the source geometry and electron energy

distribution, except that the latter needs to extend over the range corresponding to electrons that radiate synchrotron emission at frequency ν_s and IC/CMB emission at energy E_{IC} :

$$\frac{F_{\text{IC/CMB}}(\nu_{\text{IC}})}{F_s(\nu_s)} = \frac{c_2(\alpha)}{c_1(\alpha)} \frac{u_{\text{seed}}}{\nu_{\text{seed}}} B^{-(1+\alpha)} \delta^{1+\alpha} \nu_{\text{seed}}^\alpha \nu_{\text{IC}}^{-\alpha} \nu_s^\alpha. \quad (\text{A7})$$

Expressing this in more convenient units and solving for the magnetic field, we obtain

$$B = c_3(\alpha) \delta (1+z)^{(3+\alpha)/(1+\alpha)} \left(\frac{F_{s,\text{mJy}} \nu_{s,\text{GHz}}^\alpha}{F_{\text{IC/CMB},\text{nJy}} E_{\text{IC,keV}}^\alpha} \right)^{1/(1+\alpha)} \mu\text{G}. \quad (\text{A8})$$

The authors thank Dr. D. Harris for advice regarding reduction of *Chandra* data and Dr. C. Dermer for comments on a preliminary draft. This material is based upon work supported by the National Aeronautics and Space Administration under Chandra Guest Investigator grant no. GO2-3137X administered by the Smithsonian Astrophysical Observatory, and by the U.S. National Science Foundation under grant no. AST-0098579. The VLA is a facility of the National Radio Astronomy Observatory, operated by Associated Universities Inc. under cooperative agreement with the National Science Foundation.

REFERENCES

- Atoyan, A., & Dermer, C. D. 2004, ApJ, submitted, astro-ph/0402647
- Blandford, R. D., & McKee, C. F. 1977, MNRAS, 180, 343
- Celotti, A., Ghisellini, G., & Chiaberge, M. 2001, MNRAS, 321, L1
- Dermer, C. D. 1995, ApJ, 446, L63
- Dermer, C. D., & Atoyan, A. 2002, ApJ, 568, L81
- Dermer, C. D., & Atoyan, A. 2004, ApJ, submitted, astro-ph/0404139
- Dickey, J. M., & Lockman, F. J. 1990, ARA&A, 28, 215
- Gelbord, J.M. et al. 2003, BAAS, 35, 761
- Georganopolulos, M. & Kazanas, D 2004, ApJ, 604L, 81
- Gopal-Krishna, Biermann, P. L., & Wiita, P. J. 2004, ApJ, 603, L9
- Harris, D. E., & Krawczynski, H. 2002, ApJ, 565, 244
- Hartman, R. C., et al. 1999, ApJS, 123, 79
- Hewitt, A., & Burbidge, G. R. 1993, ApJS, 87, 451
- Jorstad, S. G. et al. 2001, ApJS, 134, 181
- Kellermann, K.I. et al. 2004, astro-ph/0403320
- Laing, R. A., Parma, P., de Ruiter, H. R., & Fanti, R. 1999, MNRAS, 306, 513
- Marshall, H. L., et al. 2001, ApJ, 549, L167
- Marscher, A.P. et al. 2002, ApJ, 577, 85
- Marscher, A.P. 1983, ApJ, 264, 296
- Pacholczyk, A. G. 1970, Radio Astrophysics (San Francisco: W. H. Freeman)
- Sambruna, R. M., et al. 2004, astro-ph/0401475
- Schwartz, D. A., et al. 2003, in Active Galactic Nuclei: from Central Engine to Host Galaxy, ed. S. Collin, F. Combes, & I. Shlosman, ASP Conf. Ser., in press

Shepherd, M.C. 1997, in *Astronomical Data Analysis Software and Systems VI*, ed. G. Hunt & H.E. Payne (San Francisco: ASP), ASP. Conf. Proc. 125, 77

Siemiginowska, A., et al. 2002, *ApJ*, 570, 543

Steidel, C. C., et al. 2002, *ApJ*, 570, 526

Tavecchio, F., Maraschi, L., Sambruna, R. M., & Urry, C. M. 2000, *ApJ*, 544, L23

Worrall, D. M., Birkinshaw, M., & Hardcastle, M. J. 2001, *MNRAS*, 326, L7

Table 1. **X-Ray Measurements**

	Total Counts	Net Count Rate (phot s ⁻¹)	HR^a
Core	6315±79	0.338±0.004	-0.42±0.02
C1	28±6	0.0015±0.0003	-0.43±0.24
C2	30±6	0.0016±0.0003	-0.31±0.21
C3	25±5	0.0013±0.0003	-0.76±0.25
C4	23±4	0.0012±0.0003	-0.54±0.27
Bkg	5±2	0.0002±0.0001	

Note. — ^aHardness ratio, $HR = (H - S)/(H + S)$, where S = net photon counts at 0.2-2 keV and H = net counts at 2-8 keV.

Table 2. **Parameters of Jet Features**

	X-Rays				Radio				α_r^d
	R ^a ($''$)	Φ^b ($^\circ$)	a^c ($''$)	$S_{1 \text{ keV}}$ (nJy)	R($''$)	Φ ($^\circ$)	a($''$)	$S_{5 \text{ GHz}}$ (mJy)	
Core	0.0±0.1	0.0	0.80	6185±3	0.0±0.05	0.0	0.0	1359±10	-0.39±0.02
B1 ^e	~1.0	~140	0.5±0.2	140±1	0.25±0.05	4.06±0.08	0.72±0.06
B2	2.8	146	1.5	0.66±0.21	<0.06	...
C1	4.1	150	0.7	0.77±0.21	<0.06	...
C2	4.9	151	0.7	0.91±0.23	<0.06	...
C3	5.8	157	0.9	0.82±0.21	5.6±0.2	162±2	0.80±0.05	1.2±0.1	≥1.5
C4	6.2	173	1.2	0.56±0.19	6.2±0.2	177±2	1.20±0.05	3.5±0.2	1.13±0.10
C5	<0.10	7.4±0.2	-166±2	1.50±0.05	5.4±0.3	1.13±0.06
C6	<0.10	8.1±0.2	-160±2	0.70±0.05	9.5±0.2	0.84±0.04

Note. — ^adistance from the core; ^bposition angle of knot relative to the core; ^csize of component defined as FWHM of best-fit gaussian; uncertainly in value is large, ~ 50%; ^dspectral index between 5 and 15 GHz defined as $S_\nu \propto \nu^{-\alpha}$; ^ethe X-ray characteristics of knot *B1* are not well determined owing to uncertainties in the PSF subtraction

Table 3. **Physical Parameters of the Jet: Synchrotron Model**

Knot	R''	Spine Population				Sheath Population			
		α	γ_{\min}	γ_{\max}	$B\delta$ (μG)	α	γ_{\min}	γ_{\max}	$B\delta$ (μG)
B2	2.8	0.4	10^3	3.0×10^8	5	1.5	10^2	5×10^5	< 60
C1	4.1	0.4	10^3	3.0×10^8	10	1.5	10^2	5×10^5	< 100
C2	4.9	0.4	10^3	3.0×10^8	10	1.5	10^2	5×10^5	< 100
C3	5.8	0.4	10^3	2.5×10^8	10	1.5	10^2	5×10^5	200
C4	6.2	0.4	10^3	2.5×10^8	5	1.1	10^2	5×10^5	100
C5	7.4	0.4	10^3	$\leq 1 \times 10^7$	< 3	1.1	10^2	5×10^5	90
C6	8.1	0.4	10^3	$\leq 1 \times 10^7$	< 4	0.8	10^2	5×10^5	90

Table 4. **Physical Parameters of the Jet: IC/CMB model**

Knot	R''	α	B (μG)	δ	Γ	θ ($^\circ$)
B2	2.8	0.4	2	24	24	2.4
C1	4.1	0.4	2	24	24	2.4
C2	4.9	0.4	2	24	24	2.4
C3	5.8	1.5	70	4.6	2.5	4.8
C4	6.2	1.1	60	3.3	1.8	4.8
C5	7.4	1.1	100	2.3	1.4	4.8
C6	8.1	0.8	100	2.3	1.4	4.8

Table A1. **Functions of Spectral Index α**

α	c_1	c_2	c_3	c_4	c_5	c_6	f
0.2	1.2×10^{-19}	2.7×10^{-12}	0.018	1.4	1.3×10^{-3}	1.20	0.44
0.3	8.2×10^{-18}	4.5×10^{-11}	0.036	2.5	3.1×10^{-4}	1.10	0.48
0.4	5.4×10^{-16}	7.4×10^{-10}	0.068	4.4	7.3×10^{-5}	1.04	0.52
0.5	3.5×10^{-14}	1.2×10^{-8}	0.12	7.8	1.8×10^{-5}	0.97	0.58
0.6	2.5×10^{-12}	2.0×10^{-7}	0.18	12	4.3×10^{-6}	1.00	0.64
0.7	1.7×10^{-10}	3.3×10^{-6}	0.26	20	1.0×10^{-6}	1.00	0.71
0.8	1.2×10^{-8}	5.5×10^{-5}	0.37	32	2.5×10^{-7}	1.00	0.79
0.9	8.8×10^{-7}	9.0×10^{-4}	0.49	48	6.1×10^{-8}	1.03	0.89
1.0	6.3×10^{-5}	0.015	0.64	74	1.5×10^{-8}	1.05	1.00
1.1	4.5×10^{-3}	0.25	0.82	100	3.7×10^{-9}	1.14	1.13
1.2	0.33	4.1	1.0	150	9.1×10^{-10}	1.16	1.28
1.3	23	67	1.2	210	2.2×10^{-10}	1.23	1.45
1.4	1.8×10^3	1.1×10^3	1.4	290	5.5×10^{-11}	1.29	1.65
1.5	1.5×10^5	1.8×10^4	1.6	380	1.4×10^{-11}	1.38	1.89

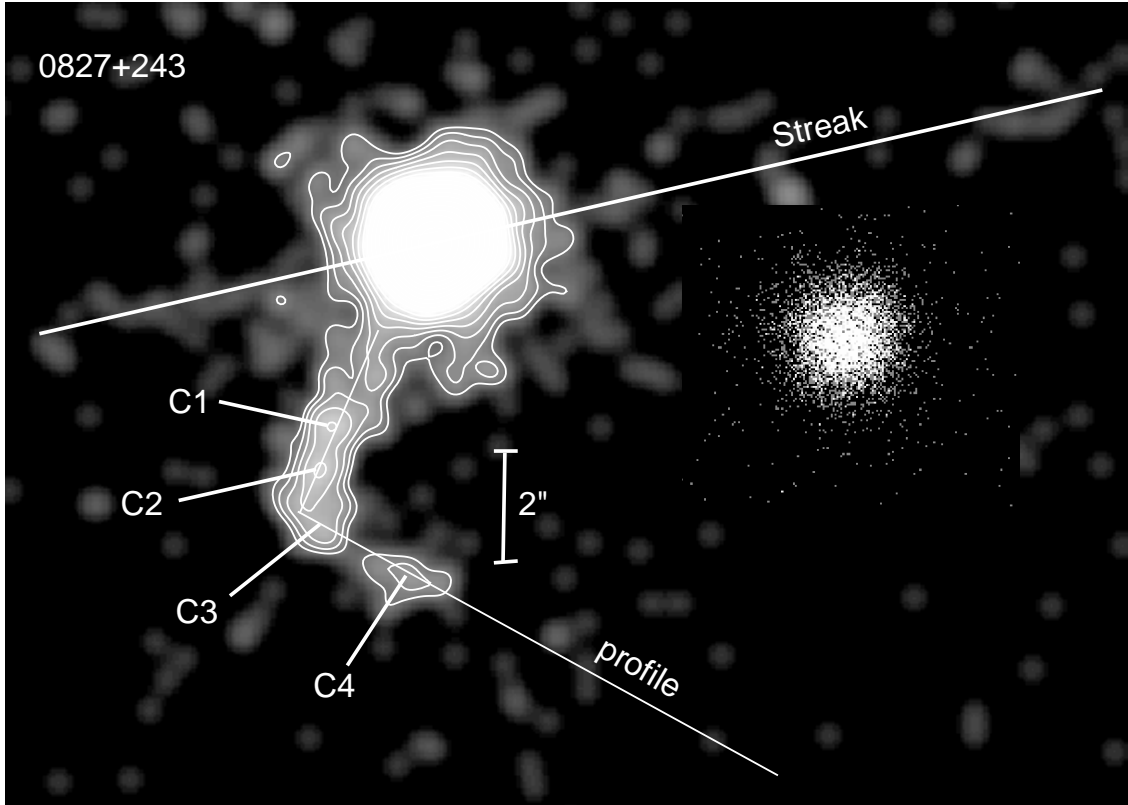


Fig. 1.— ASIC-S3 Chandra subpixelated image of 0827+243 at 0.2-8 keV convolved with a Gaussian kernel of $\sigma=0''.5$. The lines indicate positions of the readout streak and jet axis. The contour levels are in factors of 2 from 128 to 2 counts pixel^{-1} . The X-ray knots are labeled. The simulated PSF for the core region is inset on the west side of the image.

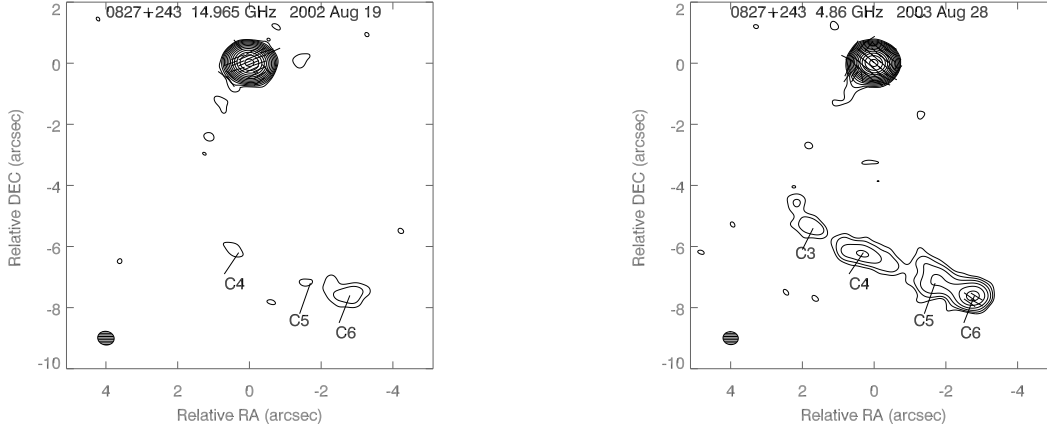


Fig. 2.— VLA images of 0827+243. The sticks indicate the direction of the electric vectors. At 15 GHz (left panel) the total intensity peak is 2.09 Jy/beam, the CLEAN beam is 0.468×0.438 arcsec² at $52^\circ 8$, the RMS is 0.075 mJy/beam, the lowest contour is 0.02% of the peak and contours increase by factors of 2. At 4.9 GHz (right panel) the total intensity peak is 1.36 Jy/beam, the CLEAN beam is 0.432×0.416 arcsec² at $48^\circ 4$, the RMS is 0.025 mJy/beam, the lowest contour is 0.01% of the peak and contours increase by factors of 2.

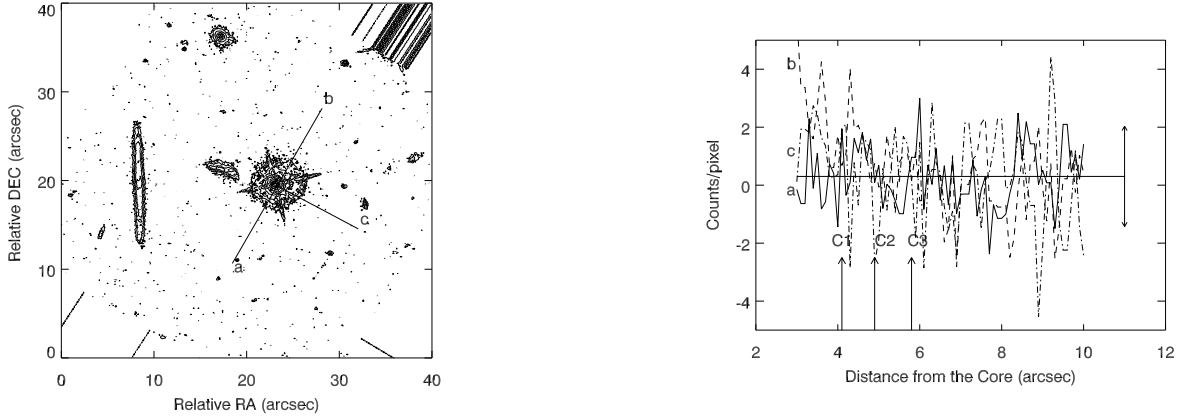


Fig. 3.— *Left panel:* *HST* image of 0827+243 with pixel size $0''.1$. The contours are in factors of 2 from 0.0001 to 0.768 of the optical peak of 3262 counts/pixel. The solid lines *a*, *b*, and *c* indicate positions of the X-ray jet, counter-jet, and control ray, respectively. *Right panel:* the optical profiles along the X-ray jet *a* (solid line), counter-jet *b* (dashed line), and control ray *c* (dash-dot line). The arrows show location of the X-ray knots. The solid straight line with arrows indicates the background level and its uncertainty.

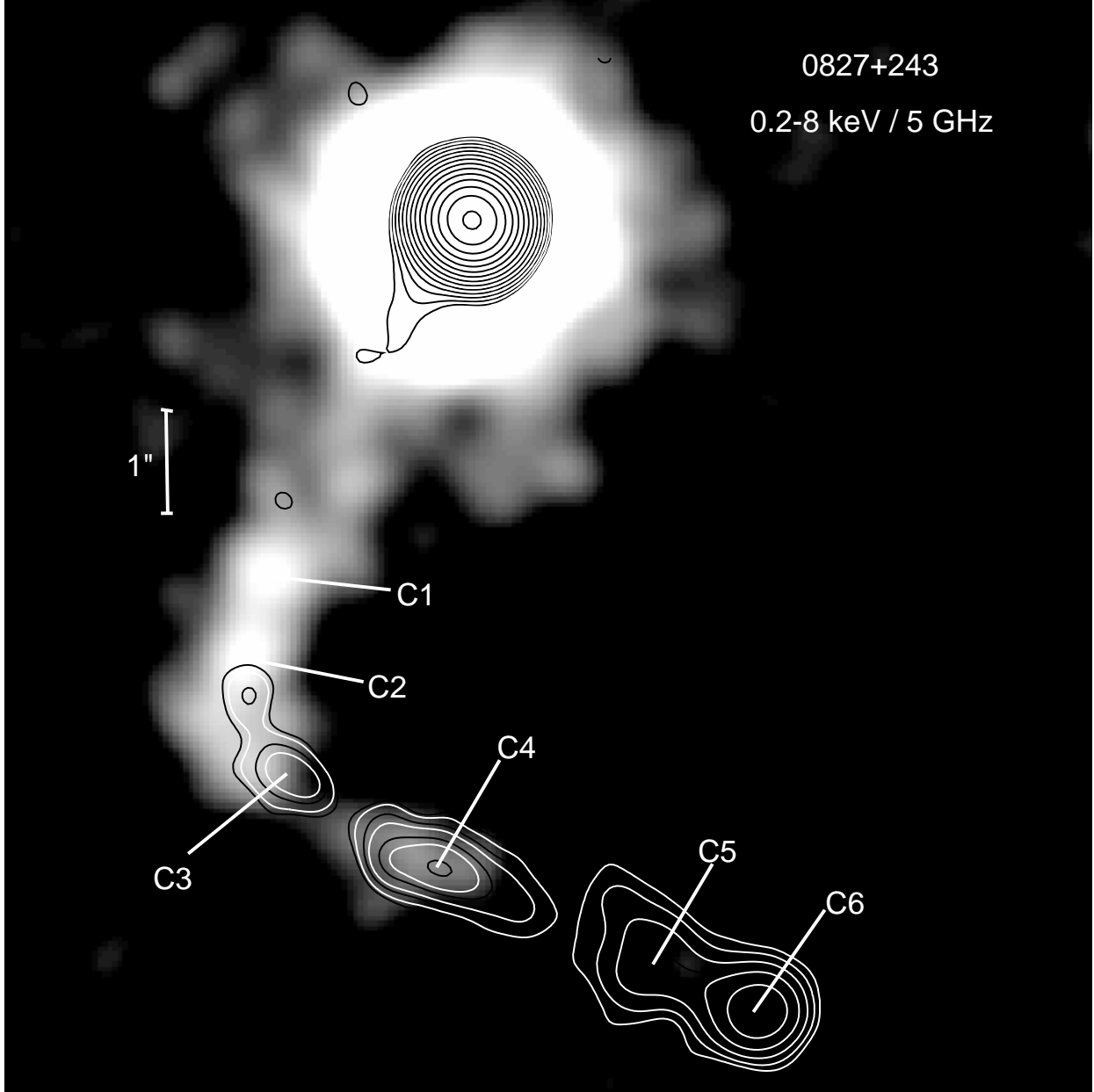


Fig. 4.— ASIC-S3 Chandra image of 0827+243 at 0.2-8 keV (gray scale) with the 4.9 GHz VLA image (contours) superposed. The images are convolved with the same Gaussian beam of FWHM $0''.5 \times 0''.5$.

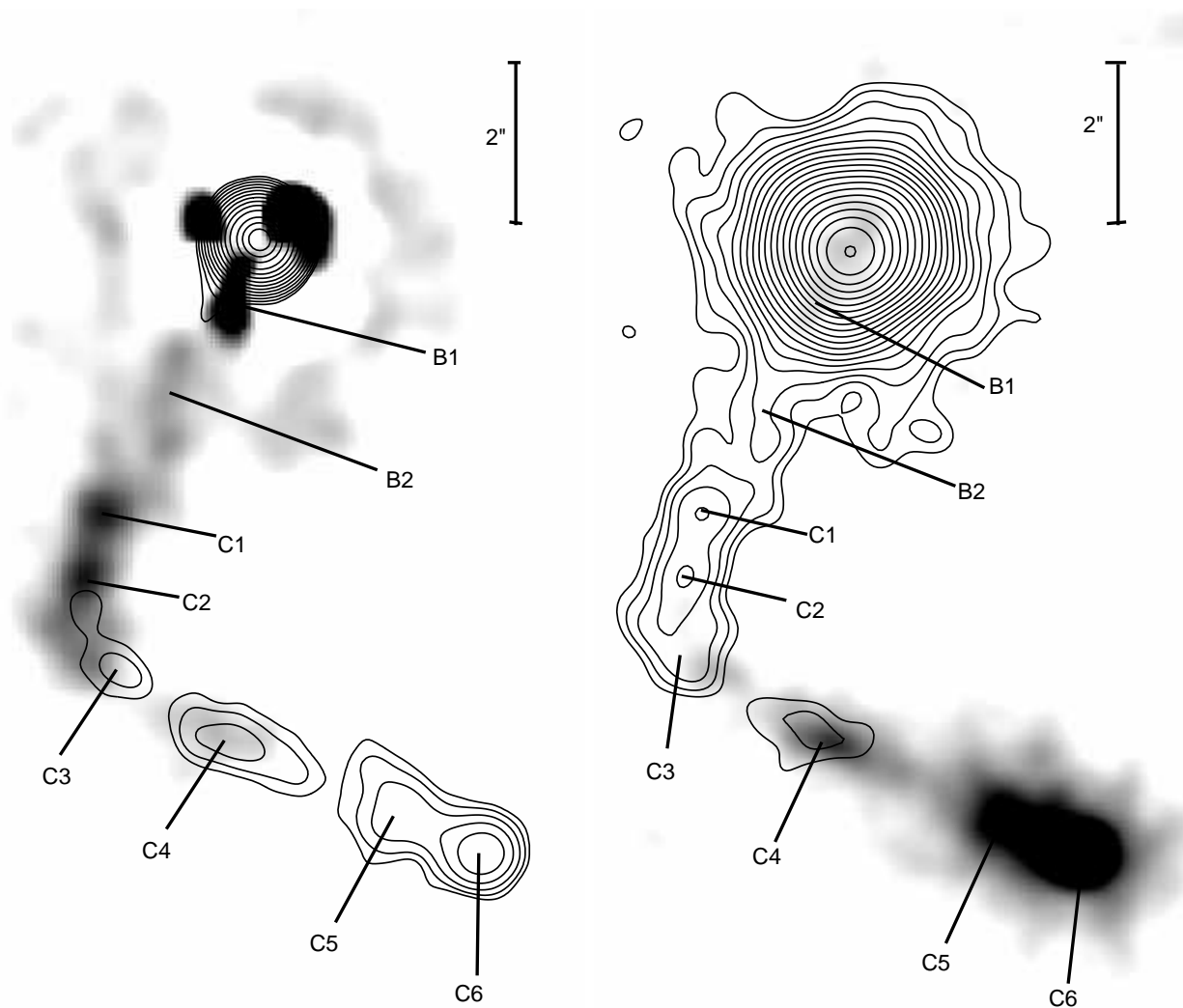


Fig. 5.— *Left panel:* ASIC-S3 Chandra image of 0827+243 at 0.2-8 keV (gray scale) deconvolved by using the PSF shown in Fig.1. The core PSF is subtracted from the image. Superposed on the image are the 4.9 GHz VLA contours (see Fig. 2). *Right panel:* VLA image of the quasar at 4.9 GHz (gray scale). The radio core is subtracted from the image after being modeled with a circular Gaussian of FWHM=0.01 mas. Superposed on the image are the X-ray contours.

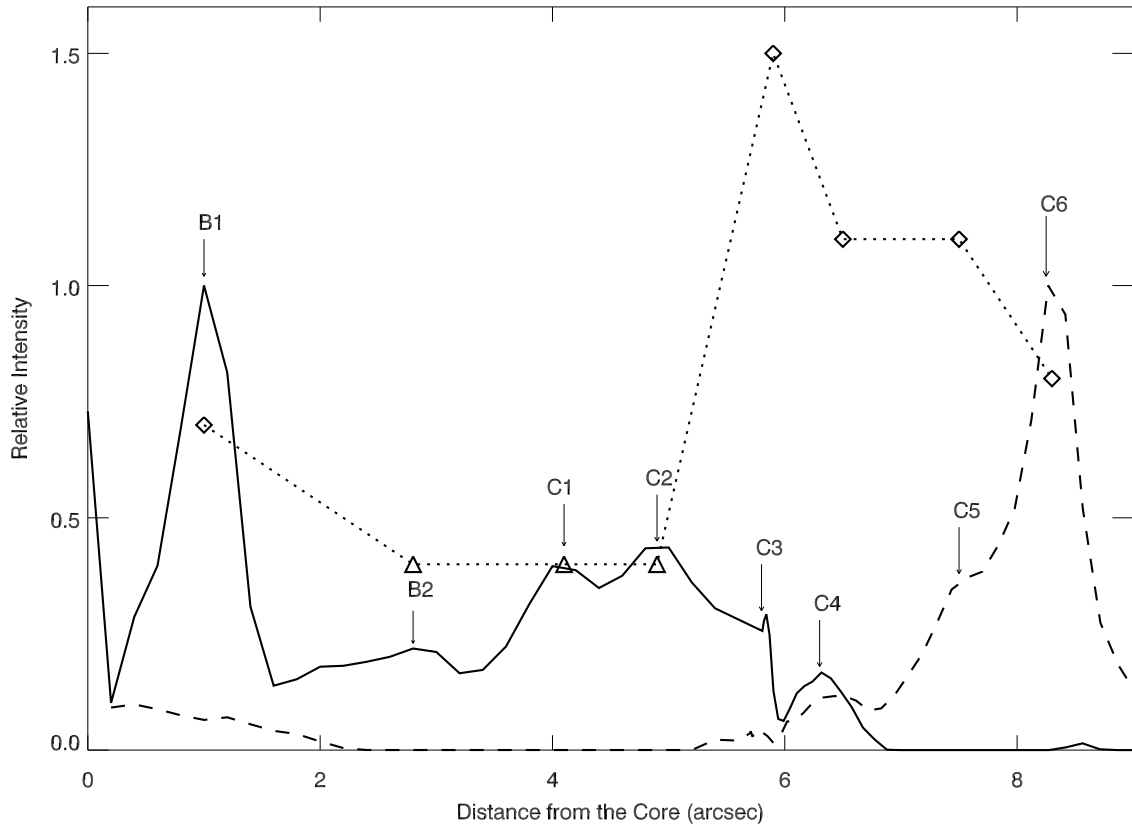


Fig. 6.— The X-ray at 0.2-8 keV (solid line) and radio at 4.9 GHz (dashed line) profiles of the jet along the axis indicated in Fig. 1. The dotted line traces the spectral index along the jet in X-ray (triangles) and between 5 and 15 GHz (diamonds).

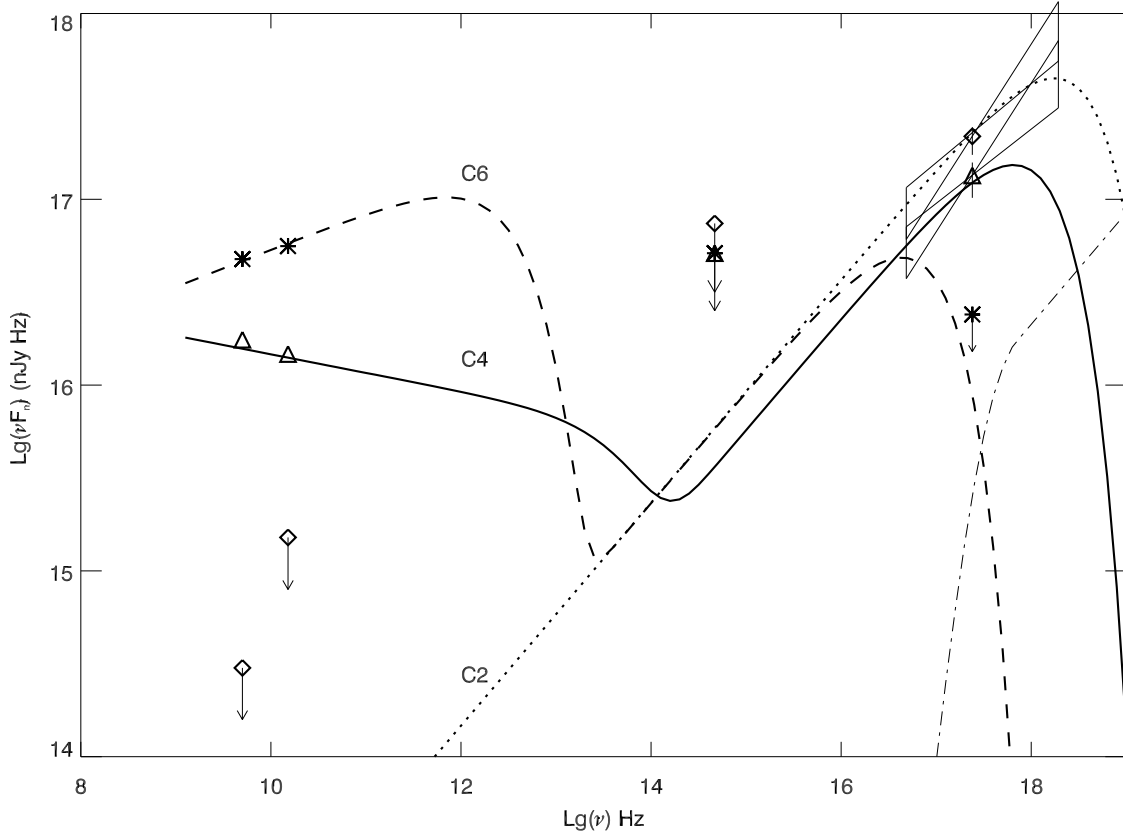


Fig. 7.— Observed spectral energy distributions (SEDs) for knots *C2* (diamonds), *C4* (triangles), and *C6* (asterisks). Curves represent simulated SEDs for combined synchrotron emission from a dual population of relativistic electrons: dotted curve for *C2*, solid curve for *C4*, and dashed curve for *C6*. The plasma parameters used to compute the model SEDs are listed in Table 3. The dash-dot curve represents the simulated SED for IC/CMB emission from the spine population with $\delta = 20$ and $B = 0.5 \mu\text{G}$.

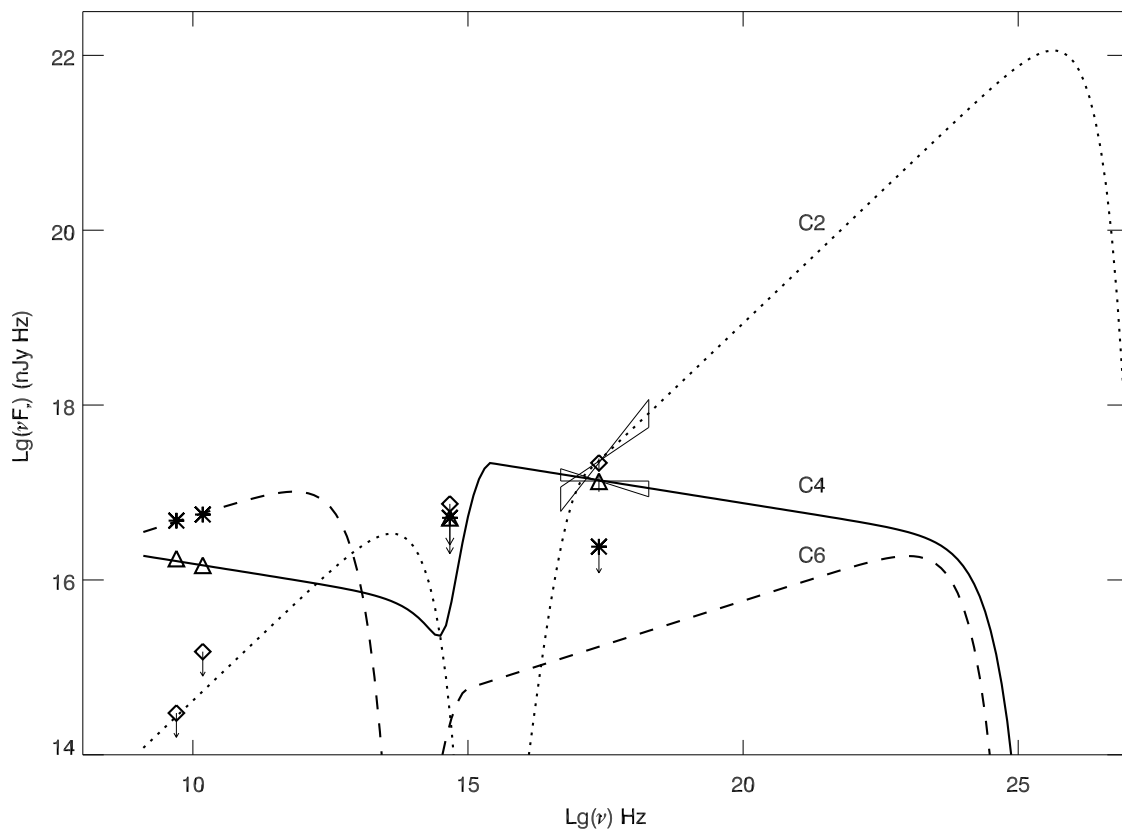


Fig. 8.— The observed spectral energy distribution for knots *C2* (diamonds), *C4* (triangles), and *C6* (asterisks). The simulated SEDs for combined synchrotron and CMB/IC emission of a single population of relativistic electrons with $\gamma_{\min} = 15$ and $\gamma_{\max} = 5 \times 10^5$ are shown by dotted curve for *C2*, solid curve for *C4*, and dashed curve for *C6*. The parameters used to compute the model SEDs are given in Table 4.

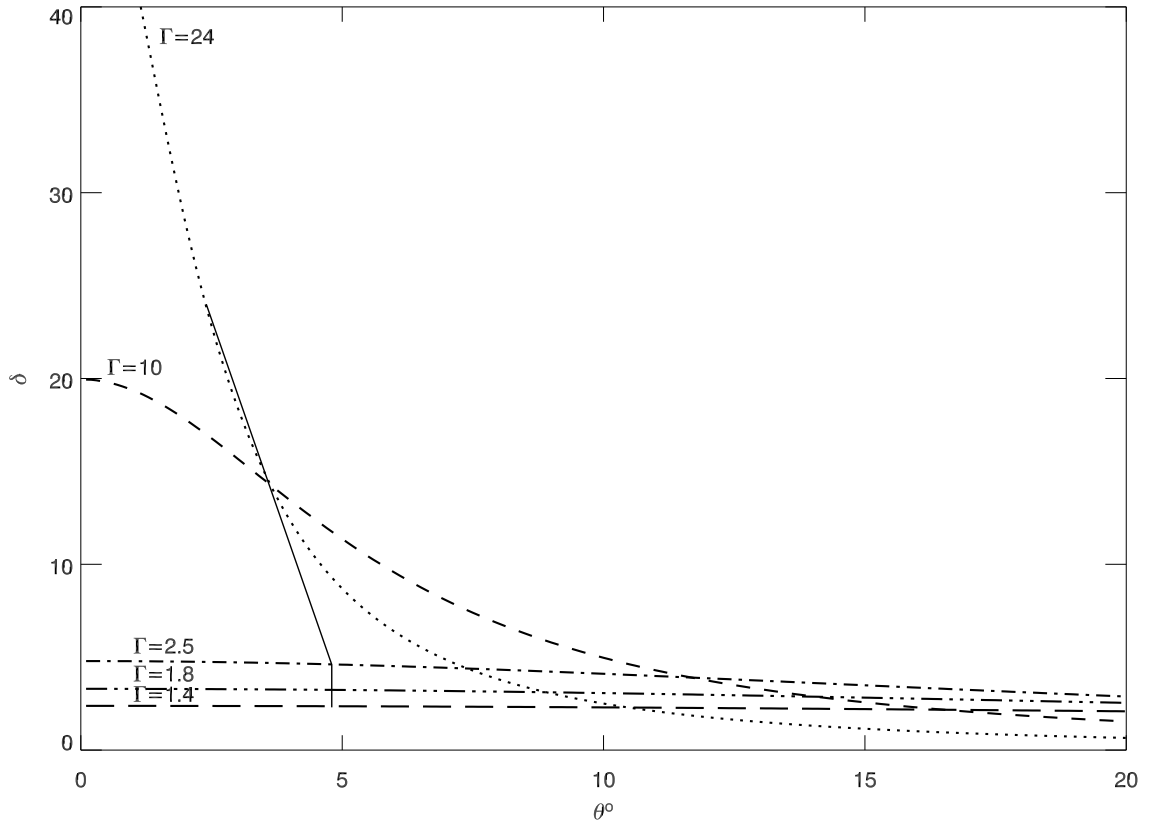


Fig. 9.— Dependence of Doppler factor on viewing angle for different bulk Lorentz factors. Broken solid line indicates how the Doppler factor might change from the core (24) to the outermost detected knot, C6 (2.3) (See Table 4).